TUTORIAL

Understanding Relaxation Oscillator Circuits Using Fast-Slow System Representations

THOMAS VOGLHUBER-BRUNNMAIER AND **BERNHARD JAKOBY**, (Fellow, IEEE)

Institute for Microelectronics and Microsensors, Johannes Kepler University, 4040 Linz, Austria

Corresponding author: Thomas Voglhuber-Brunnmaier (thomas.voglhuber-brunnmaier@jku.at)

ABSTRACT We demonstrate the utilization of the fundamental principle of nonlinear dynamics, namely, the Liénard-type representations of ordinary differential equations, also referred to as fast-slow systems, to describe and understand relaxation oscillations in electronic circuits. Relaxation oscillations are characterized by periods of slow signal changes followed by fast, sudden transitions. They are generated either intentionally by means of usually simple circuits or often occur unintentionally where they would not have been expected, such as in circuits with only one dominant energy storage device. The second energy storage required to promote oscillatory solutions of the governing equations can also be provided by spurious elements or mechanisms. The conditions that distinguish harmonic from (anharmonic) relaxation oscillations are discussed by considering the underlying eigenvalues of the system. Subsequently, we show how to intuitively understand relaxation oscillations through analyses of the phase diagram based on the fast-slow system representation of the nonlinear differential equation. Practical examples of oscillators including *RC* and *LR* op-amp circuits and the so-called "Joule thief" circuit are discussed to illustrate this principle. The applicability of the method is not limited to electrical circuits, but extends to a variety of disciplines, such as chemistry, biology, geology, meteorology, and social sciences.

INDEX TERMS Joule thief, nonlinear oscillation, phase diagram, van der Pol.

I. INTRODUCTION

Relaxation oscillators are known to electrical engineers as simple circuits and are commonly taught in undergraduate electronics courses. Fig. 1 shows one of these circuits, which utilizes an op-amp configured as an inverting Schmitt trigger and an *RC* circuit feeding the output back to the input. The principle of operation is explained by considering the capacitor-charging equation

$$V_C(t) = V_{C,\infty} + (V_{C,0} - V_{C,\infty})e^{-t/RC}, \quad (1)$$

which applies when capacitor C, with initial voltage $V_{C,0}$, is charged through resistor R. $V_{C,\infty}$ denotes the terminal voltage reached after infinite time. We assume that initially $V_C = 0$, and the output voltage of the op-amp is saturated to the maximum positive output swing V_B. The capacitor charges until V_C reaches the upper switch threshold $V_T =$

The associate editor coordinating the review of this manuscript and approving it for publication was Derek Abbott.

$V_B R_1/(R_1+R_2)$. At this point, the output voltage swings to the negative rail $-V_B$ by virtue of the positive feedback and subsequently discharges the capacitor until the negative switch threshold $-V_T$ is reached. This, in turn, causes the output to swing back to the positive supply rail. The resulting output signal is a square wave with a 50 % duty cycle. The period T is obtained using (1), by setting $V_C(T/2) = -V_T$, $V_{C,0} = V_T$ and $V_{C,\infty} = -V_B$ and solving for T yielding

$$T = 2RC \log(1 + 2R_1/R_2), \quad (2)$$

where log denotes natural logarithm. The term "relaxation" refers to the fact that the output signal shows only small, or in this case, no changes over a certain time duration but then suddenly performs a fast change, i.e., it "relaxes". While this behavior is not surprising for the shown circuit due to the hysteresis of the Schmitt trigger, relaxation oscillations also occur in circuits where no obvious discontinuous functions are involved; however, hysteresis is found as a result of some kind of nonlinear behavior.
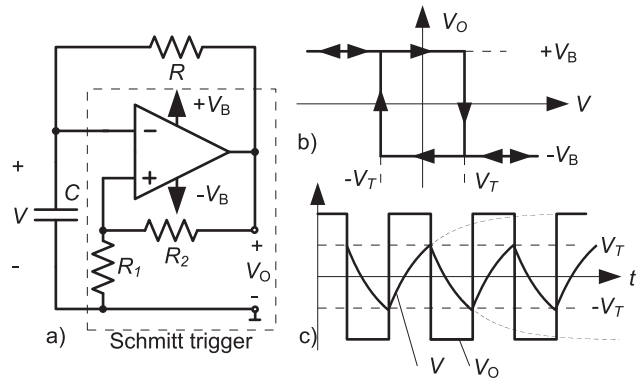
FIGURE 1. The relaxation oscillator (a) uses an inverting op-amp Schmitt trigger and an *RC* circuit. The transfer characteristic of the Schmitt trigger is shown in (b) with the switching thresholds given by $V_T = V_B R_1/(R_1 + R_2)$ (for a rail-to-rail op-amp). The capacitor voltage V oscillates between $\pm V_T$ giving a square output signal V_O.

The first formal investigation and the coining of the term ''relaxation oscillation'' can be traced back to the 1920s, when Dutch electrical engineer Balthasar van der Pol observed these phenomena in a triode vacuum tube circuit, as shown in Fig. 2 [1], [2], [3]. Although the vacuum tube circuit was expected to exhibit harmonic oscillations owing to the soft nonlinear transfer characteristic of the vacuum tube and the linearity of the remaining circuitry, van der Pol noticed the presence of relaxations.
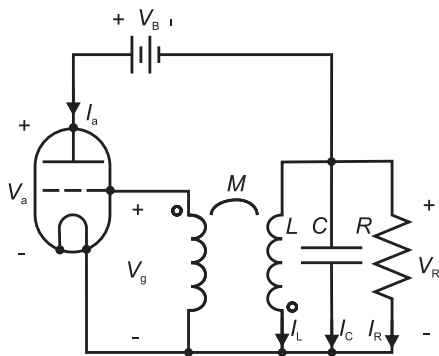

FIGURE 2. The circuit originally studied by van der Pol [1].

His formal analysis led to a deeper understanding of these phenomena, paving the way for understanding relaxation oscillations in various fields, including mechanics, biology, chemistry, and engineering problems [4]. These oscillations have been found in diverse systems such as nerve activity and heart beat [5], the Zhabotinsky reaction [6], earthquakes, prey-predator and business cycles [7], [8], climate-related cycles [9], stick-slip oscillations of bowed violin strings [8], and memristor oscillators [10], [11]. It is fascinating that simple circuit theory and basic concepts of dynamical systems are sufficient to understand these far-reaching phenomena. As such, engineers familiar with these concepts hold the key to unraveling the complexities of nature and various technological applications.

A. RLC OSCILLATOR WITH LOCAL NEGATIVE IMPEDANCE

Earlier researchers have described that harmonic signals produced by oscillators can turn into a relaxation oscillation upon the change of a specific parameter. However, this type of transition is not observed in the well-known relaxation oscillator circuit depicted in Fig. 1, particularly when idealized circuit components are considered. To explore such behavior, we first focus on the simple *RLC* tank circuit shown in Fig. 3(a) and replace resistor *R* with a negative impedance converter (NIC), as shown in Fig. 3(b) in the second step.
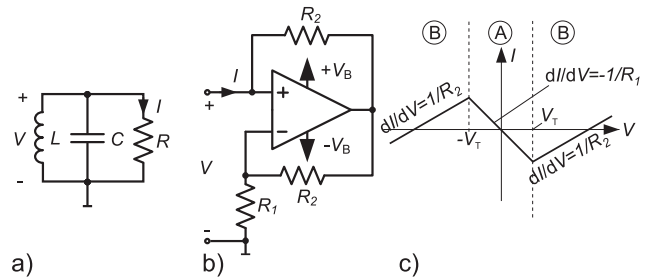
FIGURE 3. a) A simple *RLC* parallel circuit. b) The negative impedance converter (NIC) replacing *R* in circuit (a) . c) The current over voltage relation of the NIC.

When energy is initially stored in the *RLC* tank at $t = 0$, the voltage $V(t)$ will perform damped oscillations of the form

$$V(t) = Ae^{-\lambda t}\cos(\omega_g t - \phi), \tag{3}$$

when R is constant and $R^2 > L/4C$. The decay is determined by $\lambda = 1/2RC$. Amplitude A and phase ϕ depend on the initial conditions, whereas ω_g represents the angular oscillation frequency.

Theoretically, sustained oscillations require $G = 1/R = 0$. However, even a slight deviation from this value causes either an exponential decay or a growing response. A growing response is associated with a negative value of R, and can only be generated by a dedicated active circuitry. In practical systems that maintain sustained oscillations, at least two energy-storage elements and one active nonlinear element featuring locally negative impedance (compensating for unavoidable losses of the components) are required. This locally negative impedance can be realized using a so-called negative impedance converter (NIC), shown in Fig. 3(b) which features an impedance of $-R_1$ between the shown terminals, provided that the output of the op-amp is not saturated. The op-amp output (assuming a rail-to-rail op-amp) saturates at voltages $\pm V_B$ for $|V| > V_T$ with $V_T = V_B R_1/(R_1 + R_2)$. (For details on the NIC circuit, please see Appendix A and for further discussion see [12]). By attaching the NIC terminals of the circuit in Fig. 3(b) as a replacement for the resistor *R* in the tank circuit of Fig. 3(a) and applying Kirchhoff's current law at the node connecting the inductor, capacitor, and NIC, we obtain

$$\frac{dV}{dt}C + \frac{1}{L}\int dt\, V + I(V) = 0, \tag{4}$$
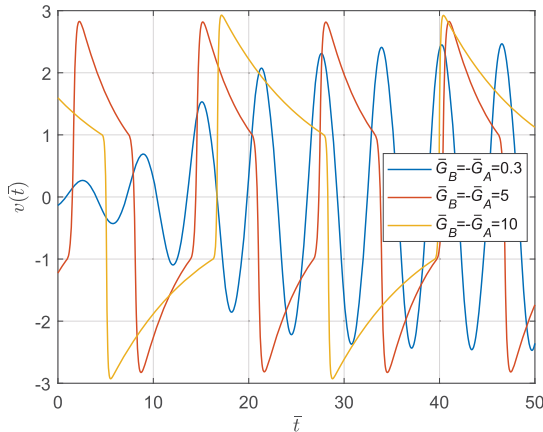
FIGURE 4. The NIC-loaded *LC* circuit performs approximately harmonic oscillations for small conductances, but the signal becomes anharmonic and shows the characteristics of relaxation oscillations.The time interval from −50 s to 0 s where the signals slowly build up, is not shown for a clearer representation of the developing steady-state signals.

FIGURE 5. Signal for nonlinear oscillator using $\bar{G}_B = -\bar{G}_A = 5$. The signal is composed by v_A (red) and v_B (blue) as given by (9) and (10). The dashed lines represent the single exponential functions in the solutions with expansion coefficients and the respective eigenvalues denoted.

which becomes after differentiation with respect to time

$$\frac{d^2V}{dt^2}C + \frac{1}{L}V + G(V)\frac{dV}{dt} = 0, \qquad (5)$$

where $G(V) = dI/dV$ represents the differential conductance and $I(V)$ is the current-voltage characteristic of the NIC, as shown in Fig. 3(c). The value of $G(V)$ changes from $-1/R_1$ (domain A in Fig. 3(c)) to $1/R_2$ (domains B) when saturation occurs. The differential equation (5) in dimensionless time $\bar{t} = t/\sqrt{LC}$, using the dimensionless differential conductance $\bar{G}(v) = G(v)\sqrt{L/C}$ is given by

$$\frac{d^2v}{d\bar{t}^2} + \bar{G}(v)\frac{dv}{d\bar{t}} + v = 0, \qquad (6)$$

where v is the dimensionless voltage $v = V/V_T$, such that $\bar{G}(|v| < 1) = -\bar{G}_A = -\sqrt{L/C}/R_1$ and $\bar{G}(|v| > 1) = \bar{G}_B = \sqrt{L/C}/R_2$. The nonlinear system can be separated into two linear systems: System A for $|v| < 1$ and System B for $|v| > 1$, featuring two different eigenvalues resulting from a solution ansatz $\propto \exp(\lambda t)$:

$$\lambda_{A\pm} = \bar{G}_A/2 \pm \sqrt{\bar{G}_A^2/4 - 1}, \qquad (7)$$
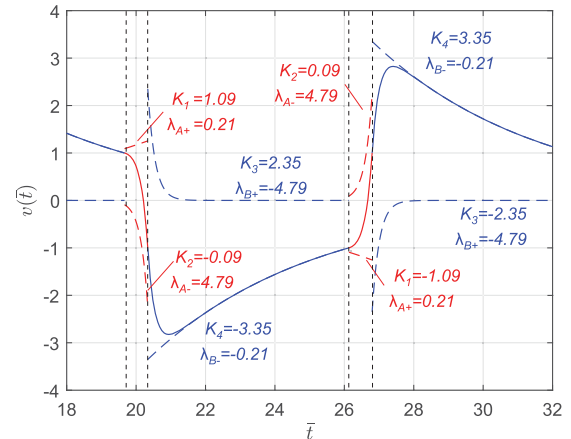
$$\lambda_{B\pm} = -\bar{G}_B/2 \pm \sqrt{\bar{G}_B^2/4 - 1}. \qquad (8)$$

The associated individual solutions are given by

$$v_A(\bar{t}) = K_1 e^{\lambda_{A-}\bar{t}} + K_2 e^{\lambda_{A+}\bar{t}}, \qquad (9)$$

$$v_B(\bar{t}) = K_3 e^{\lambda_{B-}\bar{t}} + K_4 e^{\lambda_{B+}\bar{t}}, \qquad (10)$$

with expansion coefficients K_1 to K_4. As expected from the negative impedance, function $v_A(\bar{t})$ exponentially increases with time, whereas $v_B(\bar{t})$ decays. For a particular initial condition, for example, in terms of v and its time derivative at some time, depending on what range (e.g., *A*) is associated with these conditions, the respective expansion coefficients (e.g., K_1 and K_2) can be determined. The obtained solution is valid up to the time, where v crosses the border $|v| = 1$, where the

respective other solution (*B* in our example) takes over. The coefficients (e.g., K_3 and K_4) can be determined from v and its derivative at that time. This solution is valid up to the next crossing of $|v| = 1$. Thus, the obtained partial solutions can be combined to obtain a complete solution for $v(\bar{t})$.[1] Fig. 4 shows the voltage v over dimensionless time for $\bar{G}_B = -\bar{G}_A = 0.3, 5, 10$ and the small initial condition $\bar{v}(-50) = 10^{-4}$ and $\dot{\bar{v}}(-50) = 0$. The oscillations are sinusoidal for small conductances (represented by eigenvalues that are approximately $\lambda \approx \pm j$), resulting in an angular oscillation frequency of $\omega \approx 1/\sqrt{LC}$ (that is ≈ 1 using the scaled frequency $\bar{\omega} = \omega\sqrt{LC}$). However, for larger conductances, the oscillations become anharmonic, which can be explained by considering the eigenvalues in (7) and (8): For $\bar{G}_A^2$ and $\bar{G}_B^2$ much larger than 4, the eigenvalues are real-valued, very different, and approximately given by:

$$\lambda_{A-} \approx 1/\bar{G}_A, \quad \lambda_{A+} \approx \bar{G}_A - 1/\bar{G}_A, \qquad (11)$$

$$\lambda_{B-} \approx -\bar{G}_B + 1/\bar{G}_B, \quad \lambda_{B+} \approx -1/\bar{G}_B. \qquad (12)$$

Fig. 5 shows the contributions v_A and v_B for $\bar{G}_B = -\bar{G}_A = 5$. The exponentially growing signal contribution v_A is dominated by the large eigenvalue $\lambda_{A+} = 4.79$. As outlined above, the solution v_B, composed of exponentially decaying contributions, takes over for $|v| > 1$. Somewhat unexpectedly, the signal increases further for the first moments due to the large negative eigenvalue $\lambda_{B+} = -4.79$ before it slowly decays, dominated by the smaller eigenvalue $\lambda_{B-} = -0.21$. Generally, that increasing dissimilarity of the magnitudes of the eigenvalues λ_{A-} and λ_{A+} as well as that of λ_{B-} and λ_{B+}, as $\bar{G}$ increases, causes a narrowing of the fast signal contribution v_A while dilating the slow v_B. The signal

---

[1]Note that assuming initial conditions, where both v as well as its time derivative vanish, yields the trivial solution $v = 0$. However, the slightest fluctuation in terms of noise would in reality push the system into an exponential increase in v initiating oscillations, as discussed below.
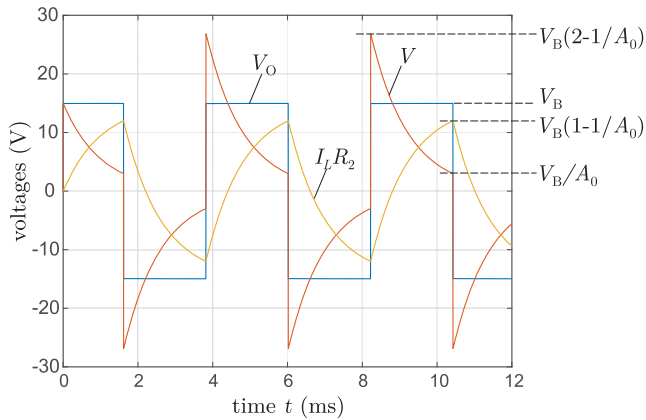
FIGURE 6. Voltage signals for the circuit shown in Fig. 3 for $V_B = 15\,V$, $L = 1\,H$, $R_2 = 1\,k\Omega$, $C \to 0\,F$, and $A_0 = 5$. To show the current I_L on one common voltage axis it is multiplied by R_2.

becomes increasingly anharmonic, which is a characteristic of relaxation oscillations.

Both dimensionless conductances $\bar{G}_A$ and $\bar{G}_B$ become large as C tends to zero, leading to very sharp transitions and extended slow parts. As the relation between dimensionless and physical time is $\bar{t} = t/\sqrt{LC}$, the slow part of the oscillation remains finite in physical time, even if C approaches zero. We refer to this situation, where the duration of the fast transition is negligible compared to the duration of the slow-part, as a fully developed relaxation oscillation. It is important to emphasize that if C is exactly zero, theoretically, only one energy-storing device remains in the circuit, and no oscillation can exist. However, in real circuits, some sort of spurious capacitance is always present, causing a fully developed relaxation oscillation.

Instead of pursuing deeper analyses of the associated differential equations (for more details see, e.g., [13]), an intuitive circuit analysis is performed to determine the characteristics of the fully developed relaxation oscillation with the resulting signals shown in Fig. 6, where it can be observed that the duration of fast transitions decreases to zero.

The circuit of the NIC in Fig. 3(b), loaded with an inductor, can also be viewed as a non-inverting amplifier with an amplification factor $A_0 = 1 + R_2/R_1$ loaded with a series circuit consisting of L and R_2. The node between L and R_2 is fed back to the positive input. From this viewpoint, the operating principle of this circuit can be derived conveniently.

Assuming that on turn-on, the output of the op-amp is saturated at the supply voltage V_B, and there is no flux in the inductor (corresponding to $I_{L,0} = 0$), such that the potential at the non-inverting input is V_B, which, for the moment, sustains the positively saturated output. Subsequently, as the magnetic field in the inductor builds up and the current starts to increase, the voltage $V = V_B - i_L(t)R_2$ across L decays exponentially until it falls below the level $V = V_B/A_0$ required to saturate the op-amp output, which causes the output, and thus, V to decrease further. This positive feedback causes the output to quickly flip to the negative

supply voltage $-V_B$. Therefore, the voltage V jumps virtually instantly from V_B/A_0 to $-V_B(2 - 1/A_0)$. After this rapid change, the current in the inductor continuously changes in the opposite direction with the same time constant as before. The associated waveforms are shown in Fig. 6. The circuit generates a square wave with a duty cycle of $50\,\%$ at the output of the op-amp. Consequently, the oscillation period is obtained using the charging equation of an LR series circuit

$$I_L(t) = I_{L,\infty} + (I_{L,0} - I_{L,\infty})e^{-tR_2/L}, \qquad (13)$$

where $I_{L,0}$ and $I_{L,\infty}$ denote the initial and terminal inductor currents, respectively, analogous to (1). Based on the working principle discussed above, (13) can be transformed to give the period T, setting $I_{L,0} = V_B(1 - 1/A_0)/R_2$, $I_{L,\infty} = -V_B/R_2$, and $I_L(T/2) = -I_{L,0}$, yielding

$$T = 2\frac{L}{R_2}\log(2A_0 - 1). \qquad (14)$$

Solving the nonlinear differential equation (6) for more complex nonlinearities is only possible using numerical methods for most problems. However, the insight gained from such an analysis is limited because important features of the oscillation (e.g., the period) cannot be directly obtained from the numerical model. Alternatively, intuitive circuit analysis reveals the operating principle and allows for the determination of the signals and oscillation periods. However, the result is accurate only for $C \approx 0$ in the previously discussed example. The waveforms are not easily obtained when, for example, the amplifier features a soft saturation curve (as will be discussed later in this paper). The main aim of this work is to illustrate the use of a third method namely analysis of the fast-slow system representation of the equations, which is illustrated for the so-called van der Pol equation first and for various other circuits later.

B. THE FAST-SLOW SYSTEM REPRESENTATION AND THE VAN DER POL EQUATION

Equation (6) represents a special case of the so-called Liénard equation [14], which can be written as

$$\frac{d^2x}{dt^2} + f(x)\frac{dx}{dt} + e(x) = 0. \qquad (15)$$

Although (6) allows for the exact solution discussed earlier, only a limited number of exact solutions to the general Liénard equation (15) are known (see, e.g., [15], [16], [17]). However, these known solutions are not directly related to circuit engineering problems; therefore, they are not discussed in this work.

The conditions for $e(x)$ and $f(x)$ in (15), for which unique and stable limit cycles exist, are obtained by considering the

equivalent problem:

$$\frac{dx}{dt} = y - F(x), \tag{16}$$

$$\frac{dy}{dt} = -e(x), \tag{17}$$

$$\text{with } F(x) = \int_0^x d\xi f(\xi), \tag{18}$$

and applying the Liénard theorem [18], which states that under the assumptions

- F and e are differentiable and odd in x,
- $xe(x) > 0$ for $x \neq 0$,
- $F(0) = 0$ and $F'(0) < 0$,
- F has a single positive zero at $x = a$,
- F increases monotonically to infinity for $x \geq a$ as $x \to \infty$

it follows that (15) has exactly one stable limit cycle.

Van der Pol derived a well-known equation based on studies of a triode vacuum tube oscillator circuit [1], as depicted in Fig. 2. Assuming a third-order polynomial transfer characteristic of the vacuum tube anode current, the dynamic equations can be transformed (see Appendix B) into the following dimensionless form [19]

$$\frac{d^2x}{d\bar{\bar{t}}^2} + \lambda(x^2 - 1)\frac{dx}{d\bar{\bar{t}}} + x = 0, \tag{19}$$

where we introduced a scaled time $\bar{\bar{t}}$ (note that this was $\bar{t}$ in Appendix B), which will be re-scaled for convenience below. This equation represents an oscillating system with amplitude-dependent damping. For $|x| < 1$, the oscillation grows, whereas it decays for $|x| > 1$, yielding a stable oscillation after the settling period. However, because the damping is time-dependent, a pure harmonic oscillation can only be obtained for $\lambda = 0$. For larger values of λ, the time signal x exhibits fast transitions.

The Liénard equation (15) is a generalization of the van der Pol equation (19) and can be represented by the so-called *fast-slow system* [20]:

$$\varepsilon\frac{dx}{d\bar{t}} = h(x, y, \varepsilon), \tag{20}$$

$$\frac{dy}{d\bar{t}} = g(x, y, \varepsilon), \tag{21}$$

where two variables, i.e., a "fast" (x) and a "slow" (y) variable appear and replace the single variable in van der Pol's equation. If x and y are vectors of dimensions m and n the system is also termed (m, n)-fast-slow system; however, in this study, we consider only (1,1)-fast-slow systems. Parameter ε is positive and much smaller than 1. Characterizing the limit cycles of this generalized representation is difficult. A reduced version of this problem, where g and h are polynomials, is known as Hilbert's 16th problem [21], which has only been partly solved to date. Even Poincaré abandoned the search for exact solutions in favor of studying qualitative features. Two important theorems are the uniqueness theorem,
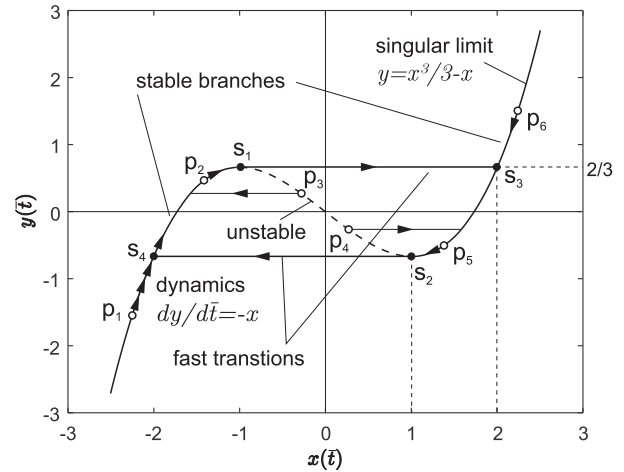
FIGURE 7. Phase diagrams for the fast-slow system representation of the van der Pol equation for different initial conditions p_1 to p_6 and $\varepsilon = 0$. The state strictly follows the singular limit and approaches either one of the two points s_1 and s_2, from which fast horizontal transitions occur also known as relaxations.

which states that trajectories in the phase diagram never intersect, and the Poincaré–Bendixson theorem [8], which states that if a trajectory is confined to a closed bounded region and there are no fixed points in the region, the trajectory must eventually approach a closed orbit.

Throughout this paper, we use the convenient representation in (20) and (21) to describe various oscillator circuits by adapting the functions h and g to fit the respective problem. To obtain this fast-slow system representation for the van der Pol equation, the so-called Liénard transform (see [20]) is applied, where the new variable y is introduced as

$$y = \int_0^x d\xi \, (\xi^2 - 1) + \frac{1}{\lambda^2}\frac{dx}{d\bar{\bar{t}}}. \tag{22}$$

The scaled time in the Liénard equation is given by $\bar{t} = \bar{\bar{t}}/\lambda$. Applying this to the van der Pol equation (19), we obtain:

$$\varepsilon\frac{dx}{d\bar{t}} = y - \frac{1}{3}x^3 + x, \tag{23}$$

$$\frac{dy}{d\bar{t}} = -x, \tag{24}$$

i.e., $h = y - x^3/3 + x$ and $g = -x$. In the context of relaxation oscillations, the parameter $\varepsilon = 1/\lambda^2$ is sometimes referred to as the "*small parameter*", as the smallness of ε corresponds to fast signal transitions. To understand the reason for this, we first study the degenerate equation, where $\varepsilon = 0$:

$$y = \frac{1}{3}x^3 - x, \tag{25}$$

$$\frac{dy}{d\bar{t}} = -x. \tag{26}$$

Setting $\varepsilon = 0$ corresponds to reducing one energy storage device in the circuit to zero. The cubic parabola in the first equation gives a strict relation between x and y in the phase diagram shown in Fig. 7 and is denoted here as the singular limit [20], whereas the second equation determines the

dynamics in the phase diagram. The degenerate system does not represent a conventional differential equation in the sense that the initial conditions cannot be arbitrarily chosen [19]. Instead, they must be points on the singular limit. For initial conditions, such as p_1 and p_2 (see Fig. 7), where $x < 0$, $\dot{y}$ is positive, causing y to tend upward until point s_1 is reached. However, s_1 is not a stable point, because x is still negative at s_1, therefore, y continues to tend upward ($dy/dt > 0$). Simultaneously, the state must remain on the curve defined by the first equation of the system. The only way to fulfill both conditions is by an instantaneous jump to the right branch of the curve, where x is positive. From here, point s_2 is approached (as now $dy/dt < 0$), where, similar as before, a jump to the left branch of the curve is induced. By eliminating y from (25) and (26), the time-derivative of x can be obtained as follows:

$$\frac{dx}{d\bar{t}} = x(t)/(1 - x(t)^2). \tag{27}$$

Instantaneous jumps occur at points $x(t) = \pm 1$. These jumps appear nonphysical and are present only because of the oversimplification by setting ε to zero. When considering specific cases, it turns out that this oversimplification is commonly associated with neglecting a component or, more generally, a mechanism that requires the system to be of second order (otherwise, a point in the phase diagram cannot reverse its direction [8]). In the case of nonzero ε, the trajectories are allowed to depart from the singular limit. This deviation is equal to h in (20), and by moving ε to the right, the expression

$$\frac{dx}{d\bar{t}} = \frac{h(x, y)}{\varepsilon} \tag{28}$$

reveals that fast transients in x (i.e., fast horizontal movements in the phase diagram) can occur, particularly for small ε.

Returning to the consideration of the degenerate system $\varepsilon = 0$, points p_3 and p_4 are expected to tend toward s_1 or s_2. However, the dashed part of the singular limit in Fig. 7 is unstable; therefore, for the initial conditions p_3 and p_4, the state jumps to the stable parts of the curve. This can be understood by considering (27). When $0 < x < 1$ then x moves in the positive x-direction and accelerates as it approaches 1. The stable parts are characterized by $\partial h(x, y)/\partial x < 0$ and the unstable parts by $\partial h(x, y)/\partial x > 0$. As pointed out in [19], these conditions can be explained kinematically in terms of the stability of the equilibrium positions of an auxiliary first-order equation by applying Liapunov's second method for stability [18]. Relaxations occur at transition points s_1 and s_2 where

$$\partial h(x, y)/\partial x = 0. \tag{29}$$

Fig. 8 shows examples for different ε values under various initial conditions. When ε is very small, fast horizontal transients occur, quickly bringing the state close to the singular limit. As the state approaches the singular limit up to a distance on the order of ε, it begins to follow the singular limit in
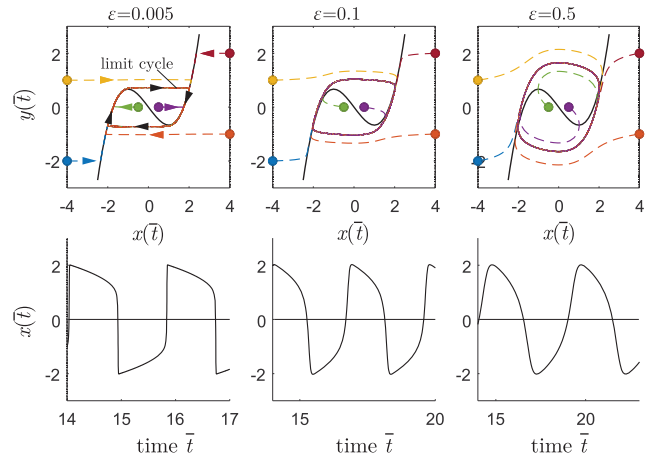
FIGURE 8. Phase diagrams for the fast-slow system representation of the van der Pol equation for different ε and the initial conditions indicated by the colored dots. Fast relaxations occur for small ε and are associated with the horizontal segments in the phase diagram.

close vicinity until it reaches the vicinity of s_1 in Fig. 7. At this point, a fast horizontal transition catapults the state against the positive arm of the singular limit, and subsequently follows the curve until it approaches point s_2. A rapid transition to the negative leg of the singular limit closes the limit cycle. Fig. 8 shows that the fast horizontal transitions become "smoother" for larger ε, which is plausible when considering that the direction of the trajectory is $dy/dx = -\varepsilon x/h$, i.e., the ratio of (26) and (28).

The oscillation frequency of the van der Pol oscillator can be estimated from the fast-slow system representation by assuming $\varepsilon = 0$ [7]. align (21) characterizes the slow signal parts, which determine the oscillation period calculated by separation of variables:

$$T = \oint_{\text{cycle}} \frac{dy}{g(x, y)}. \tag{30}$$

Here, dy is obtained from (25) and for the van der Pol oscillator this yields

$$dy = (x^2 - 1)dx. \tag{31}$$

Therefore, the dimensionless period of oscillation is [8]

$$\bar{T} = \left[\int_{s_3}^{s_2} dx + \int_{s_4}^{s_1} dx \right] \left(x^{-1} - x \right) = 3 - 2\log(2). \tag{32}$$

However, the calculation becomes much more complicated for nonzero ε. Typically, asymptotic methods such as those presented in [22] must be employed. The result in (32) is considered to be a zeroth-order approximation of such an asymptotic expansion [19]. The period of the van der Pol oscillator is known to be approximately 20% longer for $\varepsilon = 0.01$ [23], indicating that this approximation is coarse. However, in the following examples, the small parameter ε is introduced by considering spurious components, including wire inductances, the band limit of an op-amp, and the
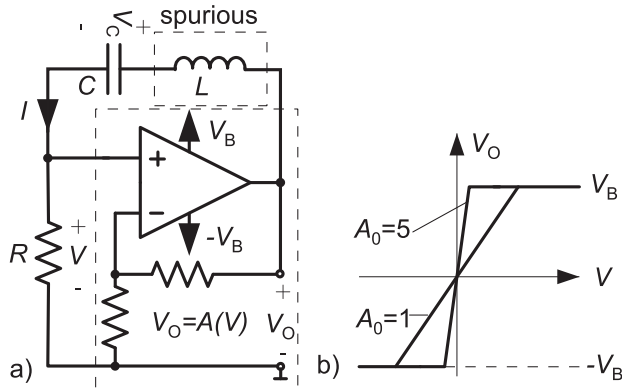
FIGURE 9. a) Relaxation oscillator using an amplifier with saturation. The small spurious inductance L is included to realize a small ε. b) The transfer function of the non-inverting amplifier is denoted by A and is shown for the two $A_0 = 1$ and 5.

FIGURE 10. Voltage waveforms for the circuit shown in Fig. 9(a) for $V_B = 15\,\text{V}$, $C = 100\,\text{nF}$, $R = 10\,\text{k}\Omega$ and $A_0 = 5$. The first peak of V is lower, as the capacitor is assumed empty at startup.

spurious capacitance of an LED. As a result, the actual ε is much smaller, and the period is accurately determined by the zeroth-order approximation.

II. VARIOUS RELAXATION OSCILLATORS

In the following sections, the transformation of the differential equations and the analysis of the fast-slow system representation, as shown in the example of the van der Pol oscillator, are applied to various oscillator circuits. These circuits include a saturating op-amp oscillator, the Schmitt trigger oscillator already introduced, and a popular simple voltage step-up converter known as the "Joule thief".

All these oscillators share the characteristic that their principle of operation can be easily understood through inspection. The oscillation frequencies of these circuits can be determined by considering the charging and discharging of capacitors and inductors. However, although establishing a simple form of nonlinear ordinary differential equations (ODEs) for each circuit is most often feasible, merely inspecting these ODEs typically does not yield the signals or oscillation frequencies as obviously as intuitive circuit analysis does. Because advanced analyses rooted in nonlinear dynamics are required to obtain these insights, understanding circuits solely by their governing equations may appear unnecessarily complicated.

Nonetheless, the transformation to a fast-slow system representation, which is easily obtained in most cases, allows for insights beyond basic circuit analysis. This representation offers a powerful tool for exploring the behavior of oscillator circuits and gaining a deeper understanding of their dynamics and characteristics.

A. RELAXATION OSCILLATOR USING SATURATION
1) BASIC CIRCUIT ANALYSIS
In Fig. 9(a), an oscillator is shown, where the op-amp in the circuit is configured as a non-inverting amplifier with moderate amplification. The limited supply voltage causes the output voltage to saturate at a certain level. The transfer
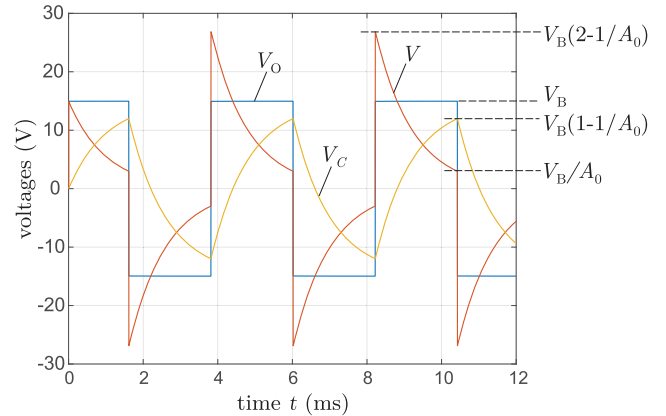
function of the op-amp with negative feedback is exemplary shown in Fig. 9(b) for two different amplification factors: $A_0 = 1$ and $A_0 = 5$. By adding capacitor C and resistor R, a positive feedback path is established.

For engineers familiar with circuit theory, the principle of operation is easily revealed by, e.g., assuming that the capacitor is initially uncharged and the output initially provides a positive supply rail voltage (assuming that a rail-to-rail op-amp is used for simplicity). As the capacitor charges, the voltage across the resistor decreases, as shown in Fig. 10. When the voltage across the resistor, which is also the input voltage of the op-amp, falls below the value required to keep the output in positive saturation, i.e., V_B/A_0, by virtue of the positive feedback of the then reducing output voltage, the output quickly swings to the negative rail $-V_B$. Because the capacitor was close to fully charged $V_C = V_B(1 - 1/A_0)$, the input voltage jumps to $-V_B(2 - 1/A_0)$. Using the RC charge equation (1) and setting $V_C(T/2) = V_B(1 - 1/A_0)$, $V_{C,0} = -V_C(T/2)$, and $V_{C,\infty} = V_B$, the period T is derived as follows:

$$T = 2RC \log(2A_0 - 1). \tag{33}$$

The equality of the wave-forms in Fig. 6 and 10 is not coincidental. The step response of the resistor voltage of an RL circuit is identical to the voltage at the capacitor in an RC series connection for equal time constants. This circuit and the circuit in Fig. 3 may be considered unusual designs because op-amps with permissible input voltages outside the supply voltage range are rare.

2) FAST-SLOW SYSTEM REPRESENTATION
To obtain a fast-slow system representation, a small parameter ε must be introduced to yield a second-order differential equation. This can be achieved, for instance, by considering a small parasitic inductance L in series with the capacitor. The ODE for current I, with $A(V)$ denoting the transfer function

of the amplifier (i.e., $V_O = A(V)$)

$$L\frac{dI}{dt} + RI + \frac{1}{C}\int dt\, I = A\,(IR), \qquad (34)$$

can be transformed into an ODE for the dimensionless input voltage $v = V/V_B$

$$\frac{d^2v}{dt^2}\frac{L}{R} + (1 - A'(v))\frac{dv}{dt} + \frac{1}{RC}v = 0 \qquad (35)$$

where $A' = dA(v)/dv$ denotes the voltage-dependent differential small-signal amplification. A similar oscillator with an additional resistor R_2 in series to C and L is discussed in [24], where it is considered a negative resistance oscillator.[2] Indeed, (35) resembles that of an RLC circuit (when multiplied by R), featuring a nonlinear resistor $R(1 - A'(v))$. For the nonsaturated op-amp, assuming $A_0 > 1$ and $4L \ll CR^2$, the eigenvalues are approximately $s_1 \approx (A_0-1)R/L$ and $s_2 \approx 0$. Therefore, waveform v builds up exponentially and is dominated by $v(t) = v(0)\exp(s_1 t)$ for an initial condition $v(0)$. Introducing a variable $x = v$ and dimensionless time $\bar{t} = t/\tau$ with $\tau = RC$ in (35) yields the following Liénard equation:

$$\varepsilon\frac{d^2x}{d\bar{t}^2} = -\left(1 - A'(x)\right)\frac{dx}{d\bar{t}} - x = 0. \qquad (36)$$

The small parameter is $\varepsilon = \tau_p/\tau$ corresponds to the ratio of the time constants $\tau_p = L/R$ to τ. Therefore, a small parameter ε also corresponds to a rapid voltage build-up during start-up. In Fig. 11, the limit cycles for three different ε values are shown, along with their associated signals. The ideal saturation characteristic $A(x)$ is shown in Fig. 12(a) for various A_0 values. $A'(x)$ in (36) is a box function, taking the value A_0 in the linear range $|x| < 1/A_0$ and 0 when saturated. The exact solution can therefore be determined by piece-wise solving of two linear ODEs while maintaining continuity at the transition points, similar to the NIC example shown before. However, a graphical approach based on a fast-slow system representation will be pursued instead. By equating $-x$ in (36) with $dy/d\bar{t}$, the variable y is defined similar to the van der Pol equation:

$$y = \int_0^x dx(1 - A'(x)) + \varepsilon\frac{dx}{d\bar{t}}. \qquad (37)$$

The integral in (37) is evaluated, yielding the associated fast-slow system representation as follows:

$$\varepsilon\frac{dx}{d\bar{t}} = y - x + A(x), \qquad (38)$$

$$\frac{dy}{d\bar{t}} = -x. \qquad (39)$$

For small spurious inductances L, ε is also small, resulting in relaxation oscillations with fast transitions. The equation is formulated in dimensionless time $\bar{t} = t/(RC)$, and the physical time axis scales with the time constant $\tau = RC$.

---

[2]It can be shown that the respective differential equation of the extended circuit can be brunnformed into (35) using the transformed quantities $v \to v/\alpha$, $R \to R_2/\alpha$, $A' \to \alpha A'$, and $V_B \to \alpha V_B$ with $\alpha = R_2/(R + R_2)$.
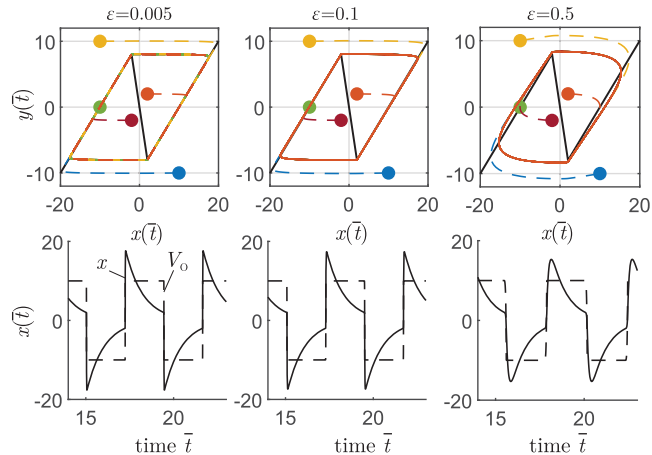
FIGURE 11. Phase diagrams for the oscillator using a saturating op-amp for supply voltage $V_B = 10\,V$ and $A_0 = 5$ and different initial conditions and ε. The input voltage swings above the power supply which requires a careful selection of the op-amp.
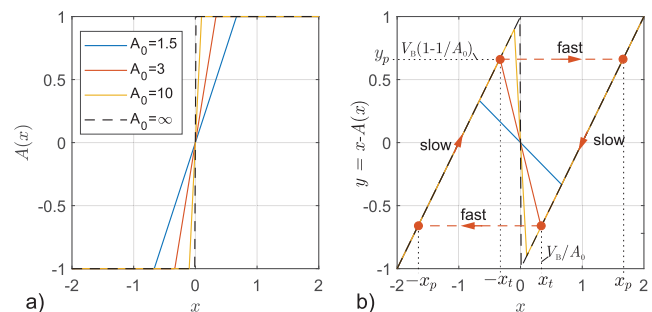
FIGURE 12. a) Transfer functions of a hard saturating amplifier for various A_0 and $V_B = 1$. b) The singular limits $y = x - A(x)$ are shown for the A_0 in (a). The transition points $\pm x_t$ and the signal maxima $\pm y_p$ are indicated for $A_0 = 3$. The left slow part is considered for the calculation of the half period of oscillation.

The singular limit, $y = x - A(x)$ is shown in Fig. 12(b) for different amplification factors. Owing to op-amp saturation, a zig-zag curve results with clearly defined transition points at $x_t = \pm V_B/A_0$, as previously found by basic circuit analysis.

The oscillation period can also be determined directly for $\varepsilon = 0$ by using (30). For $g(x, y) = -x = -(A(x) + y)$ (see (38)), and considering the left slow-part in Fig. 12, where $A(x) = -V_B$, the period in the dimensionless time frame is

$$\bar{T} = \oint_{cycle}\frac{dy}{g(x, y)} = 2\int_{-y_p}^{y_p}\frac{dy}{V_B - y} = 2\log(2A_0 - 1), \qquad (40)$$

with $\quad y_p = V_B(1 - 1/A_0). \qquad (41)$

The integration bounds $\pm y_p$ in (40) are determined by the local extrema of y at the singular limit. $A(x)$ is either V_B or $-V_B$ at the slow branches. The time constants obtained from this direct calculation and from the intuitive circuit analysis are equal when converted to the same time frame.
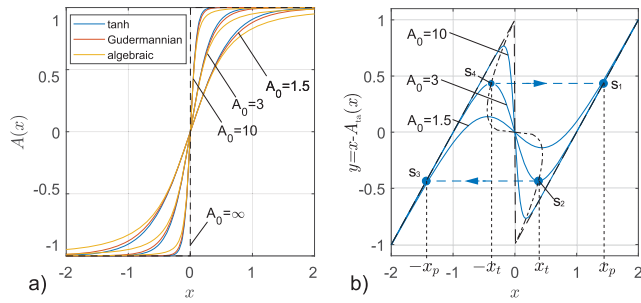
FIGURE 13. a) Transfer functions (43) to (45) of smoothly saturating amplifiers and for various A_0. b) The singular limits $y = x - A_{ta}(x)$ for the hyperbolic tangent and various A_0. The transition points s_2 and s_4 and the signal maxima are s_1 and s_3 are indicated for $A_0 = 3$. The transition points lie on the dash-dotted line for all $1 \leq A_0$, showing the high sensitivity to A_0 when it is close to 1.

For the case $A_0 = 1$ (40) yields a period of zero. However, it is apparent from (38) and (39) for $A(x) = x$, i.e.,

$$\varepsilon \frac{d^2 x}{d\bar{t}^2} = -x, \tag{42}$$

a harmonic oscillation with a period of $\bar{T} = 2\pi\sqrt{\varepsilon}$ in dimensionless time and $T = 2\pi\sqrt{LC}$ in physical time is possible; however, it is not self-exciting.

3) SOFT SATURATION

The singular limit will look more similar to that of the van der Pol oscillator if a softer saturation function of the amplifier is considered. The oscillation period of such an oscillator depends sensitively on the saturation characteristics. Three different hypothetical sigmoid functions for the transfer function of the op-amp, including a hyperbolic tangent function, Gudermannian function, and simple algebraic function that saturate at ± 1 featuring a slope of $dA/dx = A_0$ at $x = 0$, are considered:

$$A_{ta}(x) = \tanh(xA_0), \tag{43}$$

$$A_{gd}(x) = 4\arctan(\tanh(A_0\pi x/4))/\pi, \tag{44}$$

$$A_{al}(x) = \frac{A_0 x}{\sqrt{1 + (A_0 x)^2}}. \tag{45}$$

These functions are shown in Fig. 13(a) for various values of parameter A_0. For hard saturation (sharp corners of the transfer function), the differential amplification $dA(x)/dx$ jumps from A_0 to 0. However, for soft saturation, the transition points are not as obvious using basic circuit analysis, but they can be easily revealed by considering the fast-slow system representation (38) for $\varepsilon = 0$. According to (29), the transition points x_t of the singular limit shown in Fig. 13(b) are given by the local extrema of $y = x - A(x)$, associated with $dy/dx = 0$ (i.e., (38) for $\varepsilon = 0$) and hence

$$dA(x_t)/dx = 1. \tag{46}$$

Therefore, the transition points for soft saturation can be defined as, where the differential amplification drops to 1.

The input voltage thresholds x_t for the respective saturation curves are therefore

$$x_{t,ta} = \text{arsech}\left(\sqrt{1/A_0}\right)/A_0, \tag{47}$$

$$x_{t,gd} = 2\text{arsech}(1/A_0)/(A_0\pi), \tag{48}$$

$$x_{t,al} = \sqrt{A_0^{2/3} - 1}/A_0, \tag{49}$$

where arsech denotes the inverse hyperbolic secant function. The limit cycle shown in Fig. 13(b) for the hyperbolic tangent function (43) resembles that of the van der Pol oscillator, and is excited by the same mechanism. Assuming the initial condition s_1, the state approaches point s_2 from where a fast transition to s_4 is induced, followed by a slow approach to s_3. The limit cycle is closed by another fast transition. From threshold $-x_t$, an instantaneous jump to x_p occurs. x_p is therefore related to x_t by $y(-x_t) = y(x_p)$, i.e., $-x_t - A(-x_t) = x_p - A(x_p)$. This can be rearranged for x_p, yielding an attracting fixed-point iteration $x_{p,n} = A(x_t) - x_t + A(x_{p,n-1})$ as $|A'(x)| < 1$ on the slow branches. A suitable starting condition is, e.g., $A(x_{p,0}) = 1$. To obtain the exact value for the oscillation period (assuming $\varepsilon = 0$), (30) can be used:

$$\bar{T} = \oint_{\text{cycle}} \frac{dy}{g(x,y)} = -\left[\int_{s_1}^{s_2} dy + \int_{s_3}^{s_4} dy\right] \cdot \frac{1}{x} \tag{50}$$

The period in physical time is therefore given by

$$T = 2RC \int_{x_t}^{x_p} dx \frac{1 - A'(x)}{x}. \tag{51}$$

The obtained period T is a function of A_0 and scales linearly with $\tau = RC$. The numerical evaluation of the integral for various A_0 yields the results shown in Fig. 14. Surprisingly, the deviations of the periods increase with A_0, although the saturation functions appear more similar as they approach the shape of hard saturation with increasing A_0. The reason for this behavior lies in the differences of threshold voltages x_t in (47) - (49). As the capacitor discharges, its voltage tends to zero, but relaxes as it reaches x_t. Therefore, the period is particularly sensitive to x_t for large A_0. These results can be conveniently reproduced using LTspice simulation [25], as shown in Fig. 15.
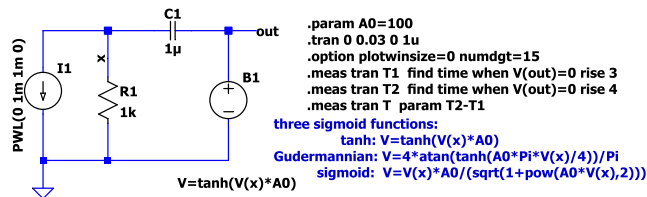
The consideration of a spurious inductance in the circuit led to the identification of the small parameter ε. It can be shown that assuming low-pass behavior of the amplifier can be used equivalently to obtain a small ε parameter. This approach is used in the following example.

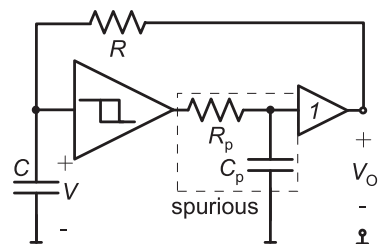### B. RELAXATION OSCILLATOR USING HYSTERESIS

In this example, the circuit discussed in the Introduction is analyzed using a fast-slow system representation. The typical interpretation of the circuit is that the capacitor voltage oscillates between the two thresholds $\pm V_T$ of the Schmitt trigger. To introduce the small parameter ε in this example, a small time constant τ_p is added to the output of the Schmitt
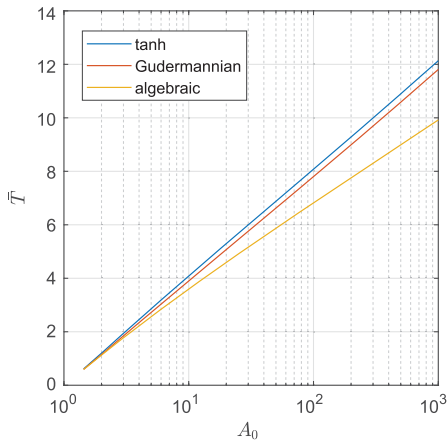
FIGURE 14. Oscillation periods in dimensionless time over A_0 for the three different saturation functions tanh (43), Gudermannian (44), and the algebraic function in (45).


```
.param A0=100
.tran 0 0.03 0 1u
.option plotwinsize=0 numdgt=15
.meas tran T1  find time when V(out)=0 rise 3
.meas tran T2  find time when V(out)=0 rise 4
.meas tran T  param T2-T1
three sigmoid functions:
    tanh: V=tanh(V(x)*A0)
Gudermannian: V=4*atan(tanh(A0*Pi*V(x)/4))/Pi
    sigmoid: V=V(x)*A0/(sqrt(1+pow(A0*V(x),2)))
```

FIGURE 15. LTspice schematic using the behavioral voltage source B1 to implement the tanh saturation characteristic in (43) for $A_0 = 100$. Replace the expression V=tanh(V(x) *A0) by one of the functions in the comments (blue text) for the other characteristics. The period of oscillation T is found in the log-file. The current source I1 provides a short current pulse at $t = 0$ to initiate the oscillation.

FIGURE 16. Relaxation oscillator using a Schmitt trigger from Fig. 1 where the small spurious time-constant $\tau = R_P C_p$ is included to realize a small ε. The transfer function of the amplifier is denoted by A.

trigger (see Fig. 16), which can be considered a first-order approximation of the slew limit or transition time of the op-amp. The buffer is added for simplicity to decouple the RC circuit from the loads. The transfer function of the trigger is denoted as $A(V)$. Circuit analysis yields the following expressions:

$$R_P C_p \frac{dV_O}{dt} = A(V) - V_O, \tag{52}$$

$$RC \frac{dV}{dt} = V_O - V. \tag{53}$$

1) FAST-SLOW SYSTEM REPRESENTATION

Introducing the dimensionless time $\bar{t} = t/\tau$ where $\tau = RC$ and $\varepsilon = \tau_p/\tau$ with $\tau_p = R_p C_p$, and using the substitutions $x = V_O/V_B$ and $y = V/V_B$ yields the fast-slow system
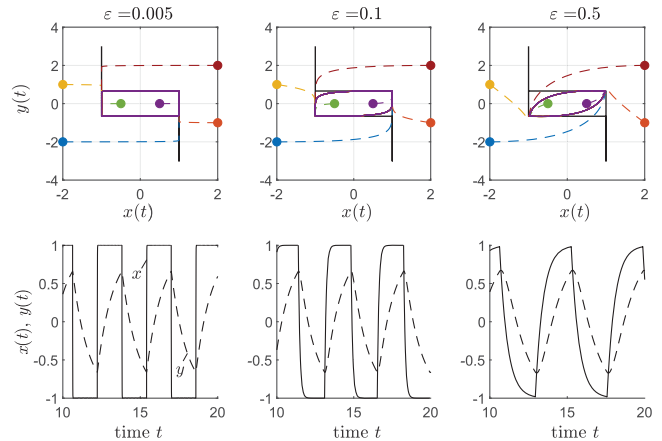
FIGURE 17. Phase diagrams for the Schmitt trigger oscillator for dimensionless threshold voltage $V_T/V_B = 0.66$ and different initial conditions and ε. The spurious output $R_P C_p$ causes the expected slower settling of the dimensionless output voltage x.

representation

$$\varepsilon \frac{dx}{d\bar{t}} = A(y) - x, \tag{54}$$

$$\frac{dy}{d\bar{t}} = x - y. \tag{55}$$

The singular limit $x = A(y)$ is shown in Fig. 17. For arbitrary initial conditions, the singular limit is quickly approached horizontally. Once in the vicinity of the singular limit, the state slowly follows the vertical segments with fast jumps between the transition points.

The formal calculation of the period from the dimensionless fast-slow system representation for $\varepsilon = 0$ yields the same result when converted to physical time, as was found by the circuit analysis in the Introduction, i.e.,

$$\bar{T} = \oint_{\text{cycle}} \frac{dy}{g(x, y)} = \oint_{\text{cycle}} \frac{dy}{A(y) - y}$$

$$= 2 \int_{-V_T/V_B}^{V_T/V_B} \frac{dy}{1 - y} = 2 \log\left(1 + 2\frac{R_1}{R_2}\right), \tag{56}$$

$$\text{with} \quad V_T/V_B = R_1/(R_1 + R_2). \tag{57}$$

C. TRANSISTOR OSCILLATOR JOULE THIEF

The term *Joule thief* refers to a simple voltage step-up converter, which as far as we know, was first presented in [26]. The circuit shown in Fig. 18, is designed to remain functional even at low battery voltages, enabling it to harvest ("steal") the last remaining bits of energy from drained batteries that are no longer useful for conventional applications. One common application of the Joule-thief is to drive an LED flashlight. The circuit's appeal lies in its low part count and relatively simple transformer design, where a few turns on a small toroid are typically sufficient for operation.
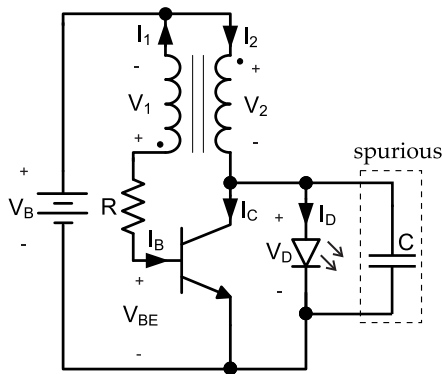
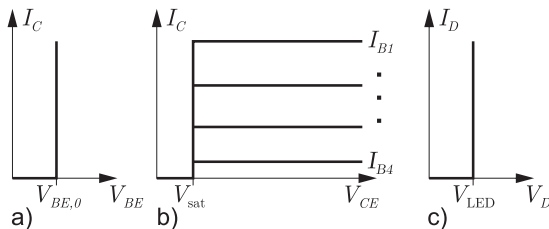**FIGURE 18.** The self-oscillating voltage step-up converter *Joule thief*.

FIGURE 19. Idealized input (a) and output (b) characteristics of transistor and LED (c). $I_C = \beta I_B$ for $V_{CE} > V_{sat}$.

1) BASIC CIRCUIT ANALYSIS

A basic circuit analysis is performed using idealized transistor and LED characteristics. The input (I_C over V_{BE}) and output (I_C over V_{CE}) characteristics of the transistor, as well as the current-voltage characteristics of the LED (I_D over V_D), are approximated by abrupt functions, as shown in Fig. 19. After connecting the battery to the circuit, a rapidly increasing small yet sufficiently large base current drives the transistor to saturation. Consequently, the voltage at the secondary side of the (tightly coupled) transformer jumps to the battery voltage V_B minus the saturation voltage V_{sat} of the transistor. Current I_2 increases linearly, as shown in Fig. 20, according to

$$dI_2/dt = (V_B - V_{sat})/L_2, \quad (58)$$

where L_2 is the inductance of the secondary winding. The primary current $I_1 = -I_B$ is small and its influence on the secondary side is neglected. The mutual inductance coupling the primary and secondary sides of the transformer is denoted by M, and the ratio of the transformer windings $N_{1,2}$ is denoted by $a = N_1/N_2$. The induced voltage $V_1 = M\dot{I}_2 = aV_2$ on the primary side enhances the base current I_B:

$$I_B = ((1 + a)V_B - aV_{sat} - V_{BE})/R, \quad (59)$$

driving the transistor further into saturation. However, when the constant base current, by virtue of the limited current gain β, is no longer sufficient to maintain the linearly increasing current I_2, the transistor opens. At this point, the collector current reaches its maximum $\hat{I}_2 = \beta I_B$. The charging time T_c is calculated using (58) by separation of variables and
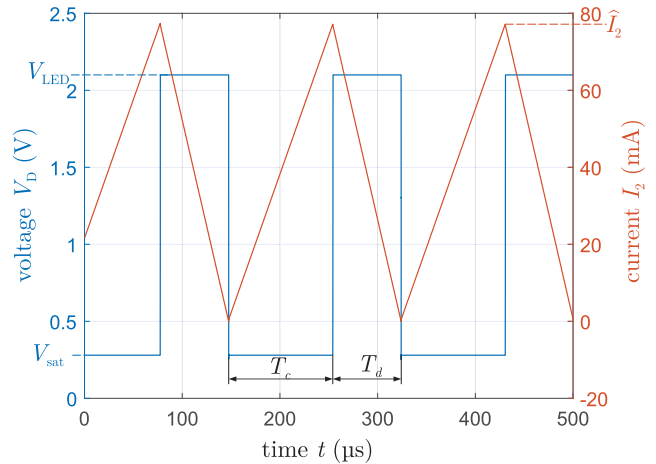

FIGURE 20. Waveforms simulated using the circuit in Fig. 21.

assuming $I_2(0) = 0$, yielding:

$$T_c = \frac{L_2 \hat{I}_2}{V_B - V_{sat}} = \beta \frac{L_2}{R} \frac{(1 + a)V_B - aV_{sat} - V_{BE}}{V_B - V_{sat}}. \quad (60)$$

After the charging interval, the voltage V_2 inverts as inductance L_2 maintains the continuity of I_2. Simultaneously, the inverted primary voltage V_1 of the transformer shuts off the transistor even more. During the discharging interval, the inductor drives the current through the LED with a forward voltage V_{LED} assumed to be constant. Consequently, $V_2 = V_B - V_{LED}$ is negative, leading to a linear decrease in I_2 according to $L_2 dI_2/dt = V_2$ until the current almost vanishes. Hence, the discharging interval T_d is given by

$$T_d = \frac{L_2 \hat{I}_2}{V_{LED} - V_B} = \beta \frac{L_2}{R} \frac{(1 + a)V_B - aV_{sat} - V_{BE}}{V_{LED} - V_B}. \quad (61)$$

The full period is $T = T_d + T_c$, and the duty cycle D can be calculated by

$$D = \frac{V_B - V_{sat}}{V_{LED} - V_{sat}}. \quad (62)$$

The current delivered to the LED decreases linearly (due to the assumption of a constant V_{LED}) from $\hat{I}_2$ to 0 during time T_d (see Fig. 20) and is zero during the charging period T_c. The RMS value of the current, denoted by $\bar{I}_D$, is calculated by

$$\bar{I}_D = \sqrt{\frac{1}{T} \int_0^{T_d} \left(\frac{\hat{I}_2}{T_d} t \right)^2 dt} = \hat{I}_2 \sqrt{D/3}. \quad (63)$$

This analysis demonstrates that the power delivered to the LED increases with higher values of a and β, and increases with a lower value of R. The most convenient method for adjusting LED power is therefore to vary R. The waveforms presented in Fig. 20 for the idealized circuit can also be simulated in LTspice by using the circuit shown in Fig. 21. The following transistor parameters are used for the simulation: $\beta = 152$, $V_{sat} = 0.28\,\mathrm{V}$ and $V_{BE} = 0.7\,\mathrm{V}$. The LED's
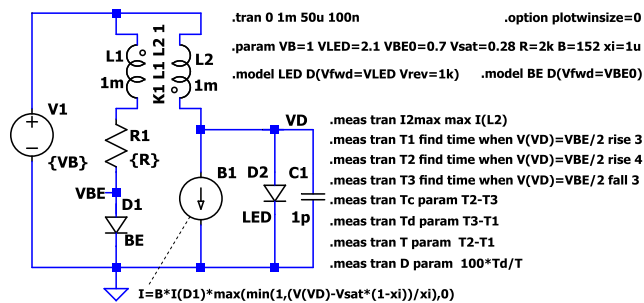
FIGURE 21. An idealized circuit simulation using LTspice utilizing a behavioral current source (xi introduces a high, but finite steepness of the saturation characteristic required for numerical stability).

FIGURE 22. The output characteristic I_C over $V_{CE}(= V_D)$ for a BC547B transistor for constant base currents I_B, simulated using the part model provided by Analog Devices, see Appendix C.

forward voltage is set to $V_{LED} = 2.1\,\text{V}$ to achieve the best agreement with the actual circuit. Note that an abrupt change in the output characteristics of the transistor when leaving saturation results in a non-converging simulation. To address this issue and ensure numerical stability, a finite steepness parameter $xi = 1\mu$ is introduced, causing the collector current to increase from zero to the maximum value within a $\Delta V_{CE} = 1\mu\text{V}$. In the simulation, a small capacitor $C1$ is incorporated into the idealized circuit to facilitate oscillations. However, its value can be as low as attofarads.

The results of this intuitive circuit analysis are approximate. In the actual circuit shown in Fig. 18, V_{sat}, V_{LED}, V_{BE}, and β change over a cycle. This introduces additional complexities that are considered using the fast-slow system representation discussed below.

2) FAST-SLOW SYSTEM REPRESENTATION

The circuit in Fig. 18 can be analyzed in the phase diagram based on the fast-slow system representation where the variations of the transistor and LED parameters during one cycle can be considered, yielding a deeper insight into the operation of the circuit. To derive the fast-slow system representation, a small parasitic capacitance C is assumed to be in parallel to the LED. By circuit simulation, it was found that considering the LED voltage $x = V_D$ and the inductor current $y = I_2$ as the fast and slow variables yields a familiar limit cycle trajectory. Using Kirchhoff's voltage law at the primary and secondary sides of the transformer, and the current law at the collector and LED node, we can establish the following relations:
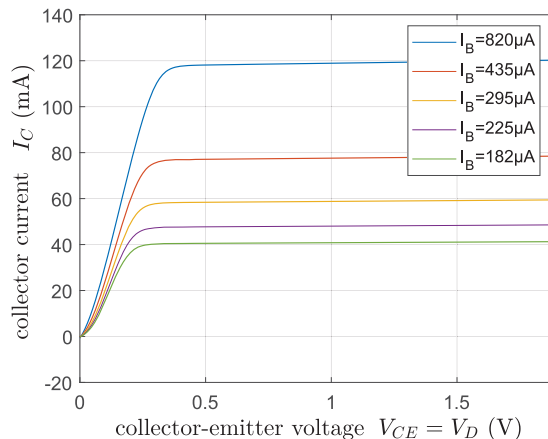
$$V_B = -V_1 + I_B R + V_{BE}, \tag{64}$$

$$V_B = V_2 + V_D, \tag{65}$$

$$C\frac{dV_D}{dt} = I_2 - I_C - I_D. \tag{66}$$

Since the current I_1 is assumed negligible, the transformer equations reduce to

$$V_1 = L_1\frac{dI_1}{dt} + M\frac{dI_2}{dt} \approx M\frac{dI_2}{dt}, \tag{67}$$

$$V_2 = M\frac{dI_1}{dt} + L_2\frac{dI_2}{dt} \approx L_2\frac{dI_2}{dt}. \tag{68}$$

The ratio $a = M/L_2$ equals the turns ratio of $N_1 : N_2$ of a tightly coupled transformer, and therefore $V_1 = aV_2$. Combining (65) with (68) yields

$$\frac{dI_2}{dt} = \frac{V_B - V_D}{L_2}, \tag{69}$$

which, together with (66), is a fast-slow system representation[3] for $\varepsilon = C$, $x = V_D$ and $y = I_2$, when the collector current I_C and the LED current I_D are expressed in terms of V_D and I_2. The base-emitter voltage V_{BE} depends on the base current $I_B(= -I_1)$ and the collector-emitter voltage V_{CE} ($= V_D$). The LED current I_D depends on the LED voltage V_D, and as driving the transistor into saturation is a crucial part of the operation principle, the collector current I_C must be considered as a function of the collector-emitter voltage and the base current, i.e.:

$$V_{BE} = F(I_B, V_D), \tag{70}$$

$$I_D = G(V_D), \tag{71}$$

$$I_C = T(V_D, I_B). \tag{72}$$

Functions F, G, and T are nonlinear and can be obtained from circuit simulations. The output characteristics of the used transistor (BC547B) $I_C = T(V_D, I_B)$ are depicted in Fig. 22 for constant base currents I_B generated using the part model included in LTspice. Using (64) and (65) with $V_1 = aV_2$ and $V_{BE} = F(I_B, V_D)$, an implicit relation between the base current I_B and the LED voltage V_D can be established as
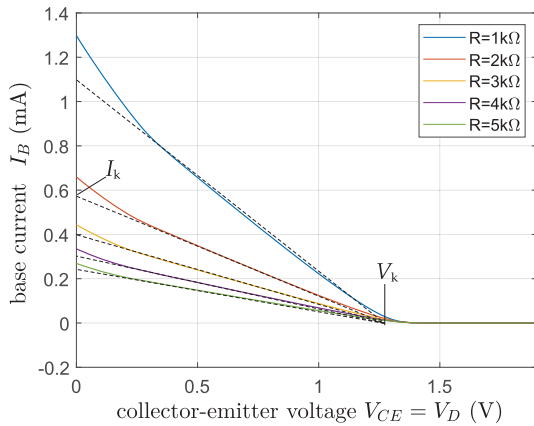
$$V_B = -a(V_B - V_D) + I_B R + F(I_B, V_D). \tag{73}$$

I_B is therefore a function of the variable V_D denoted by H, i.e.,

$$I_B = H(V_D), \tag{74}$$

which is shown in Fig. 23 for various values of resistor R in the circuit depicted in Fig. 18. The solid lines in Fig. 23

[3]In favor of easier interpretation, the variables are left in dimensional form.

FIGURE 23. The simulated relation between base current and collector-emitter voltage $I_B = H(V_D)$ following (73) for a supply voltage $V_B = 1$ V and a 1:1 transformer, i.e. $a = 1$.
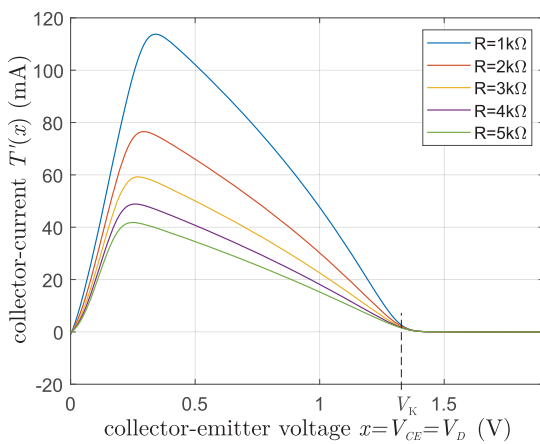

FIGURE 24. The collector current of the transistor shown in Fig. 22, when I_B is expressed as a function of the collector-emitter voltage $I_B = H(V_D)$ in Fig. 23.

are simulated, and the dashed lines are approximated using (59), assuming a constant $V_{BE} = 0.7$ V. The bends upwards at low V_D are associated with drops of V_{BE} as the usually backward biased base-collector diode begins to conduct for $V_D < V_{BE}$. The characteristic voltage V_K where the base current approaches zero, and the approximate base current for $V_D = 0$ (i.e., I_K) are therefore given by

$$V_K = \frac{V_B(1 + a) - V_{BE}}{a}, \tag{75}$$

$$I_K = \frac{aV_K}{R}. \tag{76}$$

Fig. 24 shows the collector current for various values of R under the constraint that the base current depends on $V_D(= x)$ through (74). The collector current I_C can consequently be expressed as a function of the LED voltage alone, i.e., $I_C = T(V_D, H(V_D)) = T'(V_D)$. From (66) and (69), the fast-slow
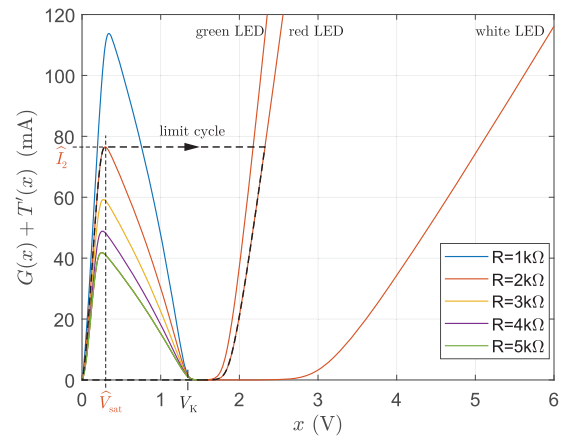

FIGURE 25. Singular limit for various values of R and three different LED types and $V_B = 1$ V and $a = 1$. A limit cycle is shown for a red LED and a base resistor $R = 2$ kΩ.

system representation

$$\varepsilon \frac{dx}{dt} = y - (T'(x) + G(x)), \tag{77}$$

$$\frac{dy}{dt} = \frac{V_B - x}{L_2}, \tag{78}$$

where $x = V_D$, $y = I_2$ and $\varepsilon = C$ is obtained. The singular limit of that system therefore is simply the sum of the collector (Fig. 24) and the LED current as a function of LED voltage x, i.e., $y = T'(x) + G(x)$, giving a typical N-shaped curve shown in Fig. 25, which is needed for relaxation oscillations to occur. Here, $T'(x)$ is shown for various values of R and $G(x)$, i.e., the voltage-current relation of the LED, is shown for LEDs of three different colors following the PSice models in Appendix C. The forward voltages of the LED are all higher than V_K (75) at which the collector current vanishes, such that transistor and LED conduct alternately. The critical point where relaxation to the right (i.e., a rapid transition) is induced is at the local maximum $\hat{I}_2$ of I_2, where the transistor leaves saturation at approximately $x = V_D \approx 0.28$ V (see Fig. 22). The base current is well-defined at this point (see Fig. 23), but the current gain β at the edge of saturation may depend sensitively on component variations. Consequently, the peak current driven through the LED, although deterministic in the simulation, may vary considerably in the experiment. Fig. 26 shows the waveforms for V_D and I_2 and Fig. 27 for V_{BE} and I_B, respectively. Compared to the waveforms in Fig. 20 of the idealized circuit, it is observed that the forward voltage of the LED and the saturation voltage change considerably over time. The secondary current I_2 depletes to zero for $V_B = 1$ V and $a = 1$. By increasing the battery voltage to, e.g., $V_B = 1.5$ V, I_2 does not deplete, as can be observed from the singular limits shown in Fig. 28. Such a condition occurs when V_K in (75) is larger than the forward voltage of the LED, which results when V_B is increased or when a (the turns ratio) is lowered to $a < 1$. The minimum secondary current and the minimum voltage V_D are nonzero in this case and are denoted by $\check{I}_2$ and $\check{V}_{\text{sat}}$, respectively.
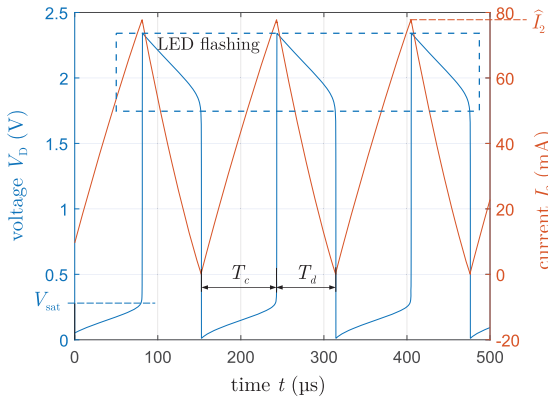
FIGURE 26. Waveforms for the Joule thief in Fig. 18 simulated using LTspice.
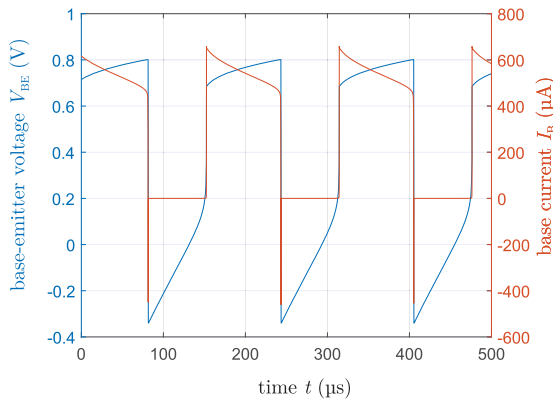
FIGURE 27. Waveforms for the base-emitter voltage and the base current.
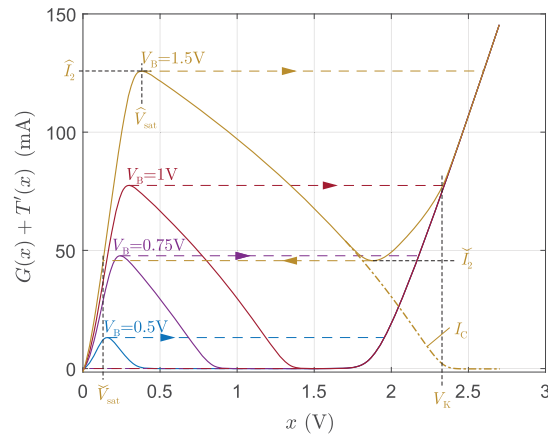
FIGURE 28. Limit cycles of the Joule thief using a BC547B with red LED and $R = 2\,\text{k}\Omega$ for four supply voltages V_B and $a = 1$. In cases where V_K in (75) is larger than the forward voltage of the LED, the current does not fully deplete.

The oscillation period is again calculated using (30):

$$T = \oint_{\text{cycle}} \frac{dy}{g(x,y)} = L_2 \oint_{\text{cycle}} \frac{d(T'(x) + G(x))}{V_B - x}. \quad (79)$$

For the left slow branch, only the transistor (corresponding to T') conducts. An improved approximation to (60) for the charging time T_c is obtained if the collector current I_C over the collector-emitter voltage V_D is linearly approximated between $V_D = 0 \ldots \hat{V}_{\text{sat}}$, i.e., $T'(x) = x\hat{I}_2/\hat{V}_{\text{sat}}$, which is justified when Fig. 24 is considered. The result is improved compared to that in (60) and reads:

$$T_c = \frac{L_2 \hat{I}_2}{\hat{V}_{\text{sat}}} \int_{\check{V}_{\text{sat}}}^{\hat{V}_{\text{sat}}} \frac{dx}{V_B - x} = L_2 \frac{\hat{I}_2}{\hat{V}_{\text{sat}}} \log\left(\frac{V_B - \check{V}_{\text{sat}}}{V_B - \hat{V}_{\text{sat}}}\right). \quad (80)$$

Here, $\hat{V}_{\text{sat}}$ denotes the peak saturation voltage, which can be obtained graphically from Fig. 25. The discharge time is calculated for the case when I_2 depletes using the diode current equation, considering the (typically considerable) series resistance R_S (see Appendix C)

$$I_D = I_S\left(\exp\left(\frac{V_D - I_D R_S}{nV_{\text{th}}}\right) - 1\right), \quad (81)$$

where V_{th} denotes the thermal voltage, and n the ideality factor. The discharge time T_d follows from the integral

$$T_d = L_2 \int_0^{\hat{I}_2} \frac{dI_D}{V_D - V_B}, \quad (82)$$

which can be evaluated numerically when (81) is transformed for V_D neglecting the 1

$$T_d = L_2 \int_0^{\hat{I}_2} \frac{dI_D}{R_S I_D + nV_{\text{th}} \ln(I_D/I_S) - V_B}. \quad (83)$$

A good approximation for (eqn:sdfkjsdhf) can be obtained:

$$T_d \approx \frac{L_2}{R_S} \ln\left(1 + \frac{\hat{I}_2 R_S}{nV_{\text{th}} \ln(\hat{I}_2/(3I_S)) - V_B}\right). \quad (84)$$

To account for a non-depleting I_2 in case of $V_B = 1.5\,\text{V}$, the lower bound in the integral (83) can be replaced by $\check{I}_2$, which, however, does not consider that there is a decreasing collector current for $V_D < V_K$ (see Fig. 25), which results in a dilation of the discharge time.[4]

In Tab. 1 the theoretical values and simulation results using the circuit in Fig. 29 are compared for a red LED and $R = 2\,\text{k}\Omega$ at various supply voltages. The power efficiency, in terms of the ratio of the average power, delivered to the LED to the average power drawn from the battery (η in Tab. 1) assuming a lossless transformer, reaches its maximum of 91.5% for $V_B = 1.28\,\text{V}$. Under these optimum conditions, the collector current does not fully vanish with $\check{I}_2 = 7.7\,\text{mA}$.

In addition to V_B and R, also the turns ratio a can be changed. Increasing a causes higher currents I_K, and with it, higher LED peak currents, which also leads to lower required

---

[4]This effect can be included, but complex expressions that are sensitive to the transistor parameters result. Therefore, the gains in terms of accuracy are limited.

TABLE 1. Simulation results for a Joule thief circuit using a BC547B transistor with $R = 2\,k\Omega$ and a red LED. The values in brackets were calculated using the respective equations given in the header of the table.

V_B	$\hat{I}_2$	$\check{I}_2$	T_c (80)	T_d (84)	$\hat{V}_{sat}$	$\bar{I}_D$ (63)	P_{avg}	D (62)	η
V	mA	mA	µs	µs	V	mA	mW	%	%
0.5	13.36	0	32.60 (31.90)	9.82 (9.73)	0.16	3.59 (3.73)	2.79	23.15 (18.48)	80.3
0.75	48.02	0	76.36 (76.42)	38.15 (38.16)	0.24	15.36 (16.01)	15.71	33.32 (28.98)	85.0
1.0	77.79	0	90.68 (90.66)	71.21 (71.11)	0.28	27.90 (29.74)	34.21	43.99 (41.86)	87.9
1.5	126.45	45.6	64.03 (62.49)	102.84 (90.60)	0.36	61.65 (57.51)	103.95	61.63 (69.51)	82.5


```
.tran 0 2m 65u 100n startup
.param R=2k     .option plotwinsize=0
.step param VB list 0.5 0.75 1 1.5
.meas tran T1 find time when V(VD) = 1 rise 3
.meas tran T2 find time when V(VD) = 1 rise 4
.meas tran T3 find time when V(VD) = 1 fall 3
.meas tran Td param T3-T1
.meas tran T param T2-T1
.meas tran Tc param T2-T3
.meas tran D param 100*Td/T
.meas I2min min I(L2)
.meas I2max max I(L2)
.meas ID_RMS RMS  I(D1)
.meas P_avg AVG  I(D1)*V(VD)
.meas Pin_avg AVG  -I(V1)*VB
.MODEL LO_541B-typ D IS=661.43E-24 N=1.6455  RS=4.8592
```

FIGURE 29. The LTspice circuit used to determine the values in Tab. 1. The results of the.meas directives are listed in the log-file of the simulation.

minimum battery voltages, which are both desirable features of a Joule thief. The turns ratio a is therefore a parameter influencing the singular limit. Increasing the inductances while keeping the turns ratio constant influences therefore only the oscillation period, provided that the inductor core does not saturate.

III. SUMMARY AND CONCLUSION

The relaxation oscillator circuits in this work were analyzed using conventional circuit analysis and graphical analysis of the phase diagram based on the fast-slow system representation. In particular, it was shown that the graphical representation of the singular limit yieldes additional insights. For instance, one can estimate the oscillation onset for an arbitrary initial condition, determine more exact expressions for the oscillation periods, or find the parameter ranges for which relaxation oscillations are excited at all. Particularly, the singular limit reveals hysteresis behavior in oscillator circuits even if there is no obvious hysteresis present in a transfer function of the circuit's building blocks.

It should be emphasized that effects associated with relaxation oscillations can be much more faceted than those presented here. For instance, a modified van der Pol system, as discussed in [7], exhibits so-called "Canard cycles" for certain parameters, where fast horizontal transitions in the phase diagram are induced not at the local maxima of the singular limits.

The examples discussed in this paper are all of order two. Higher-dimensional systems, denoted as (m, n) fast-slow system representations may show chaotic behavior for certain parameters, where no closed orbits result [13], [27].

The mathematically more involved oscillators of fractional order [28] are often encountered when distributed systems,

naturally represented by partial differential equations, are approximated using lumped elements yielding ordinary differential equations. An op-amp realization of an oscillator with fractional capacitance is discussed in, e.g., [29]).

The so-called two-stroke oscillations, known for some time [30], have recently been discussed for memristor circuits [31]. The limit cycles of these circuits show one fast and one slow transition instead of two fast and two slow transitions. The examples which were discussed in this work are therefore also referred to as four-stroke oscillators.

In summary, even though there are myriad manifestations of relaxation oscillation phenomena in natural sciences and technology worth discussing, the authors believe that electrical engineers, who add the relatively simple technique presented in this paper to their toolbox, will benefit from the possibility of viewing oscillation phenomena from a different angle and tackling problems involving nonlinear differential equations more intuitively.

APPENDIX A
THE NEGATIVE IMPEDANCE CONVERTER

In the following, the characteristics of the NIC circuit in Fig. 30 discussed in Sec. I are derived for the general case, where all resistors are potentially different.
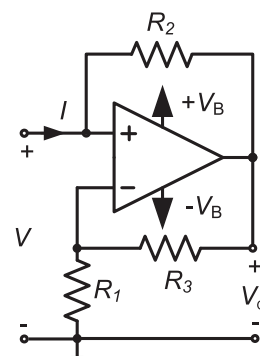
FIGURE 30. Negative impedance converter circuit.

Assuming an op-amp featuring infinite open-loop amplification and whose output is rail-to-rail, the voltage V is also present across resistor R_1 by virtue of the negative feedback. The op-amp output voltage is therefore

$$V_o = V \frac{R_1 + R_3}{R_1}. \tag{85}$$
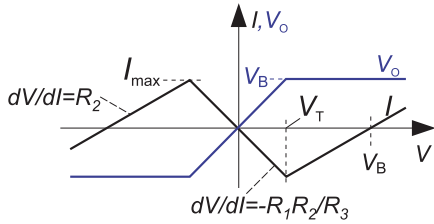
FIGURE 31. Current *I* over voltage *V* at the input terminal of the NIC circuit (black) and op-amp output voltage (blue).

As the op-amp output voltage cannot exceed V_B there is a threshold voltage for V

$$V_T = V_B \frac{R_1}{R_3 + R_1} \tag{86}$$

at which the characteristics of the NIC change. In particular, if $|V| > V_B$, the output of the op-amp will be pinned to $\pm V_B$. The input current of the NIC is therefore

$$I = \frac{V - V_o}{R_2} = -V \frac{R_3}{R_1 R_2} \text{ for } |V| \le V_T, \tag{87}$$

$$I = \frac{V - V_B}{R_2} \text{ for } V > V_T, \tag{88}$$

$$I = \frac{V + V_B}{R_2} \text{ for } V < -V_T, \tag{89}$$

and the resulting differential resistances are

$$\frac{dV}{dI} = -\frac{R_1 R_2}{R_3} \text{ for } |V| \le V_T, \tag{90}$$

$$\frac{dV}{dI} = R_2 \text{ for } |V| \ge V_T. \tag{91}$$

Fig. 31 shows the corresponding I/V characteristics. In the case of $R_2 = R_3$, as for the circuit in Fig. 3(b), it follows that the NIC features a negative resistance of $-R_1$. Maximum current $\pm I_{max}$ flows at the transition points at $\pm V_T$

$$I_{max} = \frac{V_B}{R_2} \cdot \frac{R_3}{R_1 + R_3}. \tag{92}$$

At this point also the output current from the op-amp is maximum

$$I_{O,max} = \frac{V_B}{R_2} \cdot \frac{R_2 + R_3}{R_1 + R_3} \tag{93}$$

APPENDIX B
VAN DER POL'S EQUATION
The following brief derivation of van der Pol's equation from the oscillator circuit shown in Fig. 2 follows coarsely the original paper [1]. The anode current of the triode I_a generally depends on the grid voltage V_g and the anode voltage V_a but can be approximately written as a function ϕ of a single variable, i.e., the "lumped voltage" given by $V_a + gV_g$,

$$I_a = \phi(V_a + gV_g), \tag{94}$$

where g represents the "voltage-ratio" of the tube (also known as amplification factor). The grid current is neglected.

We only consider changes around the steady, though unstable, state (i.e., $V_{a0} = V_B$, I_{a0} and $V_{g0} = 0$) and introduce the variables for the deviations v and i from these bias values:

$$v = V_a - V_{a0}, \tag{95}$$

$$i = I_a - I_{a0} = \phi(V_{a0} + v + gV_g) - \phi(V_{a0}). \tag{96}$$

The voltage at resistor V_R is related to the battery voltage V_B and anode voltage V_a by

$$V_R = V_a - V_B. \tag{97}$$

As the (tightly coupled) transformer converts only AC signals with the voltage ratio $-M/L$, the grid voltage V_g is zero-mean and therefore, $V_g = -vM/L$ and the associated variation in the anode current is

$$i = \phi(V_{a0} - kv) - \phi(V_{a0}), \tag{98}$$

with $k = gM/L - 1$. Differentiating the relation $-i = i_R + i_C + i_L$, obtained using Kirchoff's law of currents, with respect to time and using equation (97), we obtain the differential equation

$$-\frac{di}{dt} = C\frac{d^2v}{dt^2} + \frac{1}{R}\frac{dv}{dt} + \frac{1}{L}v + \frac{1}{L}(V_{a0} - V_B). \tag{99}$$

Current i can be expanded into a Taylor series around V_{a0} (using the notation $\phi' = d\phi(x)/dx$ etc.), i.e.,

$$i = -k\phi'(V_{a0})v + \frac{k^2}{2}\phi''(V_{a0})v^2 - \frac{k^3}{6}\phi'''(V_{a0})v^3 \ldots. \tag{100}$$

To obtain the van der Pol equation, it is assumed that the transfer characteristic of the tridode can be approximated in the vicinity of the steady state by using the first- and third-order terms of (100) (see Fig. 32). Therefore, the time-derivative of i is approximately given by:

$$\frac{di}{dt} = -\left(k\phi'(V_{a0}) + \frac{k^3\phi'''(V_{a0})}{2}v^2\right)\frac{dv}{dt}. \tag{101}$$

Combining equations (99) and (101) and considering that in the steady state $V_{a0} = V_B$ (because V_R is zero as there is no DC voltage drop across the inductor parallel to R) yields

$$C\frac{d^2v}{dt^2} + \left(-k\phi'(V_{a0}) + \frac{1}{R} - \frac{k^3\phi'''(V_{a0})}{2}v^2\right)\frac{dv}{dt} + \frac{1}{L}v = 0. \tag{102}$$
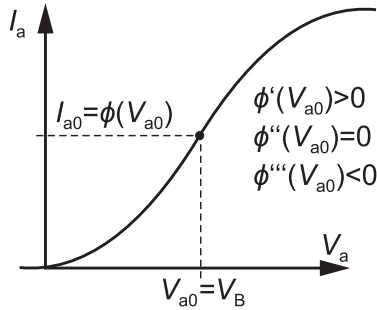
Introducing a dimensionless time $\bar{t} = t/\sqrt{LC}$ and multiplying by L yields

$$\frac{d^2v}{d\bar{t}^2} + \sqrt{\frac{L}{C}}\left(-k\phi'(V_{a0}) + \frac{1}{R} - \frac{k^3\phi'''(V_{a0})}{2}v^2\right)\frac{dv}{d\bar{t}} + v = 0. \tag{103}$$

By defining the dimensionless parameter λ as

$$\lambda = \frac{1}{R}\sqrt{\frac{L}{C}}\left(Rk\phi'(V_{a0}) - 1\right), \tag{104}$$

FIGURE 32. Assumed characteristic of the anode current I_a in equation (94) of the triode over the anode voltage V_a when the grid voltage V_g is expressed in terms of the anode voltage.

and introducing the transformed variable x

$$x^2 = v^2 \frac{Rk^3 \phi'''(V_{a0})}{2(1 - Rk\phi'(V_{a0}))}, \qquad (105)$$

finally, the van der Pol equation results:

$$\frac{d^2 x}{d\bar{t}^2} + \lambda \left(x^2 - 1 \right) \frac{dx}{d\bar{t}} + x = 0. \qquad (106)$$

Self-excited oscillations occur for the conditions $\phi'(V_{a0}) > 0$, $\phi'''(V_{a0}) < 0$ and $\lambda > 0$, i.e., $gM/L > 1 + 1/(R\phi'(V_{a0}))$.

APPENDIX C
PSpice MODELS
The model for the bipolar transistor BC547B used in the simulation is that of the manufacturer NXP and can be found in the LTspice library provided by Analog Devices Inc.

```
.MODEL BC547B NPN(IS=2.39E-14 NF=1.008~ISE=3.545E-15
NE=1.541~BF=294.3~IKF=0.1357~VAF=63.2~NR=1.004
ISC=6.272E-14 NC=1.243~BR=7.946~IKR=0.1144~VAR=25.9
RB=1 IRB=1.00E-06 RBM=1 RE=0.4683~RC=0.85~XTB=0 EG=1.11
XTI=3 CJE=1.358E-11 VJE=0.65~MJE=0.3279~TF=4.391E-10
XTF=120 VTF=2.643~ITF=0.7495~PTF=0 CJC=3.728E-12
VJC=0.3997~MJC=0.2955~XCJC=0.6193~TR=1.00E-32 CJS=0
VJS=0.75~MJS=0.333~FC=0.9579~Vceo=45 Icrating=100m
mfg=NXP)
```

The LEDs in the simulation are conventional 5mm (T1 0.75) types with the data provided by the manufacturer OSRAM.

red:

```
.MODEL LO_541B-typ D IS=661.43E-24 N=1.6455~RS=4.8592
```

green:

```
.MODEL LT_543C-typ D IS=10.000E-21 N=1.6963~RS=3.6653
```

white:

```
.MODEL LW_541C-typ D IS=414.48E-15 N=5 RS=22.499
```

REFERENCES
[1] B. van der Pol, "A theory of the amplitude of free and forced triode vibrations," *Radio Rev.*, vol. 1, no. 14, pp. 701–710, Nov. 1920.

[2] B. van der Pol, "On 'relaxation-oscillations,'" *London, Edinburgh, Dublin Philos. Mag. J. Sci.*, vol. 2, no. 11, pp. 978–992, 1926.

[3] J.-M. Ginoux and C. Letellier, "Van der Pol and the history of relaxation oscillations: Toward the emergence of a concept," *Chaos, Interdiscipl. J. Nonlinear Sci.*, vol. 22, no. 2, Jun. 2012, Art. no. 023120.

[4] D. Wang, "Relaxation oscillators and networks," in *Wiley Encyclopedia of Electrical and Electronics Engineering*, vol. 18. Hoboken, NJ, USA: Wiley, 1999, pp. 396–405.

[5] G. Buzsáki and A. Draguhn, "Neuronal oscillations in cortical networks," *Science*, vol. 304, no. 5679, pp. 1926–1929, Jun. 2004.

[6] S. M. Blagojević, S. R. Anić, Ž. D. Čupić, N. D. Pejić, and L. Z. Kolar-Anić, "Malonic acid concentration as a control parameter in the kinetic analysis of the Belousov–Zhabotinsky reaction under batch conditions," *Phys. Chem. Chem. Phys.*, vol. 10, no. 44, pp. 6658–6664, 2008.

[7] J. Grasman, "Relaxation oscillations," in *Mathematics of Complexity and Dynamical Systems* R. A. Meyers, Ed. New York, NY, USA: Springer, 2011, pp. 1476–1477.

[8] S. H. Strogatz, *Nonlinear Dynamics and Chaos: With Applications to Physics, Biology, Chemistry, and Engineering*. Boca Raton, FL, USA: CRC Press, 2018, p. 212, 203, 28, and 214.

[9] M. Crucifix, "Oscillators and relaxation phenomena in pleistocene climate theory," *Phil. Trans. Roy. Soc. A, Math., Phys. Eng. Sci.*, vol. 370, no. 1962, pp. 1140–1165, Mar. 2012.

[10] F. Corinto, A. Ascoli, and M. Gilli, "Nonlinear dynamics of memristor oscillators," *IEEE Trans. Circuits Syst. I, Reg. Papers*, vol. 58, no. 6, pp. 1323–1336, Jun. 2011.

[11] A. Ascoli, S. Slesazeck, H. Mähne, R. Tetzlaff, and T. Mikolajick, "Nonlinear dynamics of a locally-active memristor," *IEEE Trans. Circuits Syst. I, Reg. Papers*, vol. 62, no. 4, pp. 1165–1174, Apr. 2015.

[12] A. Pilipenko and V. Biryukov, "Investigation of modern numerical analysis methods of self-oscillatory circuits efficiency," *J. Radio Electron.*, vol. 8, pp. 1–9, Aug. 2013.

[13] M. P. Kennedy, "Three steps to chaos. I. Evolution," *IEEE Trans. Circuits Syst. I, Fundam. Theory Appl.*, vol. 40, no. 10, pp. 640–656, Oct. 1993.

[14] A. Liénard, "Etude des oscillations entretenues," *Revue Generale l'Electricite*, vol. 23, pp. 901–902, 1928.

[15] J. Freitag, R. Jaoui, D. Marker, and J. Nagloo, "On the equations of Poizat and Liénard," 2022, *arXiv:2201.03838*.

[16] T. Harko and S.-D. Liang, "Exact solutions of the Liénard- and generalized Liénard-type ordinary nonlinear differential equations obtained by deforming the phase space coordinates of the linear harmonic oscillator," *J. Eng. Math.*, vol. 98, no. 1, pp. 93–111, Jun. 2016.

[17] Z. Feng, "On explicit exact solutions for the Lienard equation and its applications," *Phys. Lett. A*, vol. 293, nos. 1–2, pp. 50–56, Jan. 2002.

[18] L. Perko, *Differential Equations and Dynamical Systems*, vol. 7. New York, NY, USA: Springer, 2013, p. 254 and 129.

[19] E. Mishchenko, *Differential Equations with Small Parameters and Relaxation Oscillations*, vol. 13. New York, NY, USA: Springer, 2013, p. 7, 13, 17, and 45.

[20] C. Kuehn, *Multiple Time Scale Dynamics*, vol. 191. Cham, Switzerland: Springer, 2015, pp. 8–12.

[21] S. Lynch, "Symbolic computation of Lyapunov quantities and the second part of Hilbert's sixteenth problem," in *Differential Equations with Symbolic Computation*, D. Wang and Z. Zheng, Eds. Basel, Switzerland: Birkhäuser, 2005, pp. 1–22.

[22] J. Grasman, *Asymptotic Methods for Relaxation Oscillations and Applications*, vol. 63. New York, NY, USA: Springer, 2012.

[23] J. J. Stoker, *Nonlinear Vibrations in Mechanical and Electrical Systems*, vol. 2. New York, NY, USA: Wiley, 1950, p. 141.

[24] A. B. Pippard, *The Physics of Vibration*. Cambridge, U.K.: Cambridge Univ. Press, 2007, p. 327.

[25] Analog Devices Inc. *LTspice*. Wilmington, MA, USA. Accessed: Jul. 30. [Online]. Available: https://www.analog.com/en/design-center/design-tools-and-calculators/ltspice-simulator.html

[26] Z. Kaparnik and W. Swindon, "One volt LED—A bright light," *Everyday Practical Electron. (EPE) Mag.*, p. 804, Nov. 1999.

[27] M. P. Kennedy, "Three steps to chaos. II. A Chua's circuit primer," *IEEE Trans. Circuits Syst. I, Fundam. Theory Appl.*, vol. 40, no. 10, pp. 657–674, Oct. 1993.

[28] F. Mainardi, "Fractional relaxation-oscillation and fractional diffusion-wave phenomena," *Chaos, Solitons Fractals*, vol. 7, no. 9, pp. 1461–1477, Sep. 1996.

[29] O. Elwy, A. M. Abdelaty, L. A. Said, A. H. Madian, and A. G. Radwan, "Two implementations of fractional-order relaxation oscillators," *Anal. Integr. Circuits Signal Process.*, vol. 106, no. 2, pp. 421–432, Feb. 2021.

[30] P. Le Corbeiller, "Two-stroke oscillators," *IRE Trans. Circuit Theory*, vol. 7, no. 4, pp. 387–398, 1960.

[31] J.-M. Ginoux, R. Meucci, S. Euzzor, and A. D. Garbo, "Torus breakdown in a two-stroke relaxation memristor," *Chaos, Solitons Fractals*, vol. 153, Dec. 2021, Art. no. 111594.

THOMAS VOGLHUBER-BRUNNMAIER received the M.S. and Ph.D. degrees in mechatronics from Johannes Kepler University (JKU), Linz, Austria, in 2007 and 2013, respectively. From 2007 to 2008, he worked in the research and development of gas-flow sensors with small enterprise. From 2008 to 2012, he was a University Assistant (Ph.D. position) with the Institute for Microelectronics and Microsensors (IME), JKU. From 2012 to 2013, he was a Senior Scientist with the Austrian Center of Competence in Mechatronics (ACCM), Linz. From 2013 to 2016, he was with the Department for Integrated Sensor Systems, Danube University Krems. From 2016 to 2017, he was a Project Leader with the Linz Institute of Technology (LIT). Since 2015, he has been a Senior Researcher with IME. He has also been the Patent Scout of mechatronics with the IPR Department, JKU, since 2018, and was the Deputy Head of the IPR, from 2020 to 2022. His research interests include the modeling of fluid sensors, measurement science, and electrical circuit engineering. He received the Anerkennungspreis OVE, in 2022; the AMA Innovation Award, in 2020; the AMA Young Enterprise Award, in 2020; the International Mechatronics Award MEC, in 2014; the OGMA/OVE Award, in 2013; and the ARGE Sensorik Special Award, in 2011.

BERNHARD JAKOBY (Fellow, IEEE) received the Dipl.-Ing. (M.Sc.) degree in communication engineering, the Ph.D. degree in electrical engineering, and the Venia Legendi degree in theoretical electrical engineering from the Vienna University of Technology (VUT), Austria, in 1991, 1994, and 2001, respectively. From 1991 to 1994, he was a Research Assistant with the Institute of General Electrical Engineering and Electronics, VUT. He stayed as an Erwin Schrödinger Fellow with the University of Ghent, Belgium, performing research on the electrodynamics of complex media. From 1996 to 1999, he was a Research Associate and later an Assistant Professor with the Delft University of Technology, The Netherlands, working in the field of microacoustic sensors. From 1999 to 2001, he was with the Automotive Electronics Division, Robert Bosch GmbH, Germany, where he was conducting development projects in the field of automotive liquid sensors. He joined the newly formed Industrial Sensor Systems Group, VUT, as an Associate Professor, in 2001. He was appointed as a Full Professor of microelectronics with Johannes Kepler University, Linz, Austria, in 2005, where he is currently working in the field of sensors. He was elected as a Eurosensors Fellow, in 2009, and a Full Member of the Austrian Academy of Sciences, in 2022. He received the Outstanding Paper Award 2010, for a paper in the IEEE Transactions on Ultrasonics, Ferroelectrics and, Frequency Control, in 2010. He served as the Technical Co-Chair, the Co-Chair, and the General Chair for various conferences, including the IEEE Sensors Conference and the I2MTC. He is also an Editorial Board Member of the IEEE Sensors Journal, *Sensors and Actuators A*, and *Measurement Science and Technology*.

• • •